DOI: 10.1002/ejic.200700181

Synthesis and Characterization of Silver-Nanoparticle-Deposited α-$Bi_2Mo_3O_{12}$ Nanorods

Anil Vithal Ghule,[a] Kalyani Ghule,[a] Shin-Hwa Tzing,[a] and Yong-Chien Ling*[a]

Keywords: Nanoparticles / Ultrasound / Deposition / Nanorods / Surface analysis / Electron microscopy

Silver (Ag) nanoparticles with an average size of ca. 10 nm were uniformly deposited on the surface of α-$Bi_2Mo_3O_{12}$ nanorods by using an ultrasound sonication method. Ultrasonic irradiation of preformed α-$Bi_2Mo_3O_{12}$ spherical nanoparticles (ca. 200 nm) in pyridine resulted in α-$Bi_2Mo_3O_{12}$ nanorods (ca. 100 nm diameter). Further, sonication of the mixture of α-$Bi_2Mo_3O_{12}$ nanorods and Ag_2O in pyridine yielded a nanocomposite of α-$Bi_2Mo_3O_{12}$ nanorods with deposited Ag nanoparticles and pyridine. Calcination of the nanocomposite at 450 °C afforded pyridine-free α-$Bi_2Mo_3O_{12}$ nanorods with deposited Ag nanoparticles. A plausible mechanism is proposed. The crystallized Ag nanoparticles are uniformly deposited on the surface, with bismuth (Bi) as the preferential binding site, as revealed by time-of-flight secondary ion mass spectrometry (TOF-SIMS). Structural, compositional and morphological characterization of the products is carried out by using transmission electron microscopy, energy-dispersive X-ray analysis, scanning electron microscopy, thermogravimetric analysis, X-ray diffraction, X-ray photoelectron spectroscopy and TOF-SIMS.

Introduction

Since last decade, the science and technology of nanomaterials has created immense interest in their potential technological applications. This has inspired the synthesis of nanomaterials of various shapes and sizes including nanoparticles, nanotubes, nanorods, nanoribbons, nanowires, nanospheres, nanocrystals, nanoflasks and so on, composed of metals, metal oxides, organic, inorganic and bioinorganic compounds, and their hybrid composites.[1] The category of hybrid nanocomposites in general has broadened significantly to encompass a large variety of systems and is a fast-growing area of research. Layered inorganic compounds have been studied for a considerable time as candidates for the generation of nanohybrids. This area is enjoying a resurgence of interest and activity as a result of the exceptional properties that can be realized from these nanocomposites. Because inorganic layered materials exist in great variety with a well-defined ordered intralamellar space, they serve as hosts accessible to guest species and yield interesting hybrid nanocomposites. Significant efforts are focused on the ability to obtain control of the nanoscale structures by judiciously engineering the host–guest interactions through innovative synthetic approaches. This has enabled the synthesis of nanocomposites with a broad range of properties. The properties of nanocomposites depend not only on the properties of their individual parents, but also on their morphology and interfacial characteristics. As the remarkable properties of conventional composites are mainly due to interface interactions, any system that is subjected to critical analysis is of interest. Although selected classes of these composites may be amenable to direct structural characterization by standard crystallographic methods, an important issue in this area is the limited availability of structural and morphological details. Furthermore, nanocomposites also offer the possibility to combine diverse properties, which is impossible within a single material; thus, they promise new applications in many fields.

Bismuth, molybdenum and their oxides have been explored with great interest for technological applications.[2] However, very little attention was focused on binary oxides, despite their wide applicability. Bismuth molybdates (α-$Bi_2Mo_3O_{12}$, β-$Bi_2Mo_2O_9$ and γ-Bi_2MoO_6) are popular and widely explored catalysts of commercial importance.[3] Furthermore, bismuth–molybdenum-based oxides have also found applications as pure oxide ionic conductors,[4] as optical[5] and acousto–optical materials,[6] as photoconductors in thin films,[7] and as gas sensors in breath-analyzer devices.[8] Modification of the surface properties plays an important role in the behaviour of these compounds; thus, increased effort has been made to modify their surfaces to create new classes of compounds with different properties.[9]

Ag dispersed on metal oxides is gaining popularity as a catalyst.[10] Moreover, Ag has low hardness and wear resistance, and thus it is often alloyed with other metals to improve its properties.[11] For example, Ag–Bi alloys have gained importance as they find applications in electronics, lead-free soldering, radiotechnics and in the production of

[a] Department of Chemistry, National Tsing Hua University, Hsinchu, Taiwan 30013
Fax: +886-3-5711082
E-mail: ycling@mx.nthu.edu.tw

coatings exposed to severe conditions, for example, friction under high pressure.[12] The use of Ag films as a buffer layer for the preparation of Bi-2212 tapes on Ni, Ni–Cr, stainless steel and Hastelloy substrates has also been exploited with great interest.[13] Thus, by banking on the information that Ag has a good interaction with Bi, Ag was selected for deposition on α-$Bi_2Mo_3O_{12}$ nanorods in this work. It was also of interest to investigate the mode of interaction and preferred binding site of Ag on the surface of the α-$Bi_2Mo_3O_{12}$ nanorods, which would provide useful information for the design of novel composite materials with improved properties.

Various methods, including wet chemistry techniques, colloid reduction chemical routes, inverse micelle and surfactant utilization, electrochemical and electroless plating, sol-gel and spray pyrolysis etc., have been employed to modify or coat the substrates with noble metals, and complicated apparatus are usually required. In contrast, sonochemistry is a simple alternative technique, which has been exploited extensively to coat nanoparticles and prepare a variety of metal nanoparticles and oxide nanorods.[14,15] Herein, we use a simple ultrasound method[16,17] to deposit Ag nanoparticles on the surface of α-$Bi_2Mo_3O_{12}$ nanorods. To the best of our knowledge, this is the first report of this procedure.

Results and Discussion

Sonochemistry is gaining importance for its simplicity in the synthesis of nanomaterials and coating nanoparticles on substrates.[18] Power ultrasound effecting chemical changes by cavitation phenomena that involves the formation, growth and implosive collapse of bubbles in liquid, is exploited in this technique.[17] Synthesis of metal nanoparticles by using ultrasound techniques is well reported.[14] Furthermore, sonication of the precursor nanoparticles in the presence of an inorganic support such as α-$Bi_2Mo_3O_{12}$ nanorods provides a means of trapping the nanoparticles by chemical affinity to produce heterogeneous catalysts. Herein it is exploited to deposit Ag nanoparticles on the surface of α-$Bi_2Mo_3O_{12}$ nanorods by using pyridine as a medium.

The motivation for the use of pyridine in this work comes from the extensive studies conducted on pyridine intercalation with bismuth molybdate as substrates, where mostly hydrated forms were used as starting material.[19–21] The use of the hydrated form of bismuth molybdate adds to the controversy and thus the anhydrous form is used in this work, the details of which are discussed elsewhere.[16,22] Moreover, no change in the composition of the substrates was reported or observed by us with the use of pyridine.[16,22] In contrast, sonication of α-$Bi_2Mo_3O_{12}$ in water and NH_4OH (pH of 8) results in the formation of MoO_3 nanorods and nanoribbons instead of the formation of α-$Bi_2Mo_3O_{12}$ nanorods. This is confirmed by transmission electron microscopy (TEM) images, energy dispersive X-ray analysis (EDS) spectra and selected area electron diffraction (SAED) patterns (data not shown).[16] This supports the importance of pyridine in α-$Bi_2Mo_3O_{12}$ nanorod formation. Furthermore, it was observed that the intercalation and adsorption of pyridine on the surface of α-$Bi_2Mo_3O_{12}$ nanorods helps to retain its phase without degradation to form mixed phases.[16] Extensive reports on the adsorption of pyridine on metal surfaces also exist,[23] which provides active sites for chemical manipulation of the surfaces. This N-containing aromatic compound has generated particular interest because of its useful physical and chemical properties that are derived from the lone pair of electrons on the N atom. Pyridine molecules are adsorbed on the surface predominantly through metal–N dative bonding and to oxygen as pyridinium or pyridinium oxide.[16,24] The pyridine molecules orient themselves perpendicular to the surface and parallel to each other.

Electron Microscopy

Scanning electron microscopy (SEM) and TEM are used for morphological characterization of Ag-nanoparticle-deposited α-$Bi_2Mo_3O_{12}$ nanorods and also to investigate the nature of the adherence of the particles to the surface. The SEM and TEM micrographs of Ag nanoparticles that are deposited on α-$Bi_2Mo_3O_{12}$ nanorods obtained after sonication for 60 min are shown in Figure 1a and b, respectively. The Ag nanoparticles, which are about 10 nm in size, deposit uniformly on the surface of α-$Bi_2Mo_3O_{12}$ nanorods as shown in Figure 1b. The inset of Figure 1b shows a TEM image of Ag nanoparticles (ca. 10 nm size) obtained on sonication of Ag_2O in pyridine for 60 min. Figure 1c shows a high-resolution TEM micrograph of a Ag nanoparticle. Crystallinity of the Ag nanoparticles is confirmed by the lattice fringes and lattice spacing, which are characteristic of Ag. The lattice spacing is noted to be 0.235 nm for the (111) plane and is in agreement with earlier reports.[25] To further confirm the crystallinity of the Ag nanoparticles, SAED patterns and EDS spectra were also recorded. The SAED pattern of a single Ag nanoparticle is shown in the inset of Figure 1c. It shows diffused rings with *d* spacing 0.235 [111], 0.144 [220], 0.118 [222] and 0.091 [420], which is characteristic of FCC silver metal and in agreement with the International Center for Diffraction Data file #03-0931. For better comparison, EDS spectra from (i) α-$Bi_2Mo_3O_{12}$ nanorods, (ii) α-$Bi_2Mo_3O_{12}$ nanorods coated with Ag nanoparticles and (iii) a single Ag nanoparticle are recorded as shown in Figure 1d. The presence of silver, bismuth, molybdenum, oxygen and copper is confirmed from the α-$Bi_2Mo_3O_{12}$ nanorods that contain deposited Ag nanoparticles [Figure 1d, spectrum (ii)], whereas the EDS spectrum procured from a single Ag nanoparticle shows the exclusive presence of Ag [Figure 1d, spectrum (iii)].

Experiments with an increased sonication time (90 and 120 min) were also conducted and showed aggregation of Ag nanoparticles possibly because of forced excess collapse of Ag nanoparticles with increased sonication time. The representative TEM micrograph of Ag nanoparticles aggre-

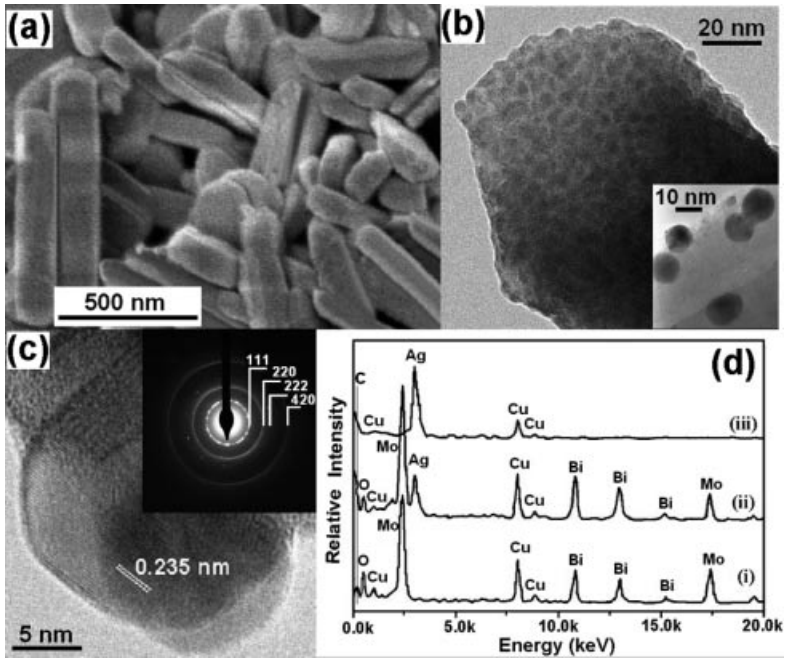

Figure 1. (a) SEM and (b) TEM micrographs of α-$Bi_2Mo_3O_{12}$ nanorods with deposited Ag nanoparticles obtained after sonication for 60 min. Inset shows Ag nanoparticles (ca. 10 nm) obtained from sonication of Ag_2O in pyridine for 60 min. (c) HRTEM image of a single Ag nanoparticle, indicating the size of ca. 10 nm and showing lattice fringes characteristic of metallic Ag. The inset is the characteristic SAED pattern obtained from the Ag nanoparticle. (d) Representative energy-dispersive X-ray analysis spectra (EDS) of (i) α-$Bi_2Mo_3O_{12}$ nanorods, (ii) α-$Bi_2Mo_3O_{12}$ nanorods with deposited Ag nanoparticles showing the presence of Bi, Mo, Ag and O and (iii) a single Ag nanoparticle.

gated on α-$Bi_2Mo_3O_{12}$ nanorods obtained after sonication for 120 min is shown in Figure 2a. When the amount of Ag_2O is varied (200 and 300 mg) with the use of the same amount of α-$Bi_2Mo_3O_{12}$ nanorods (2 g) and a sonication time of 60 min, the number of deposited Ag nanoparticles increased. Figure 2b shows a representative TEM micrograph of one end (tip) of Ag nanoparticles deposited α-$Bi_2Mo_3O_{12}$ nanorods obtained from the use of 300 mg of Ag_2O and a sonication time of 60 min. The Ag nanoparticles appear to be localized in close vicinity with minimal aggregation; however, the particle size is observed to be same (ca. 10 nm) unlike that observed after an increased sonication time (Figure 2a). It appears that subsequently deposited Ag nanoparticles are directed to the voids of the previously deposited nanoparticles (inset in Figure 2b) as a result of pyridine being adsorbed on the surface. It is also observed that the number of free Ag nanoparticles in the product increases with increased amounts of Ag_2O. Figure 2c shows a TEM image of randomly deposited Ag_2O nanoparticles on the surface of α-$Bi_2Mo_3O_{12}$ nanorods obtained from vigorous stirring of the mixture of Ag_2O and α-$Bi_2Mo_3O_{12}$ nanorods at 40 °C for 60 min. The size of the deposited and free nanoparticles in the product is larger and the particles are confirmed to be of Ag_2O. The XRD pattern obtained from the product shows characteristic peaks at 2θ = 32.85°, 38.10°, 55.01° and 65.57°, which can be indexed to [111], [200], [220] and [311] reflection lines, respectively, of Ag_2O particles (JCPDS 75-1532). Additionally, chains of large Ag_2O particles are also observed in the

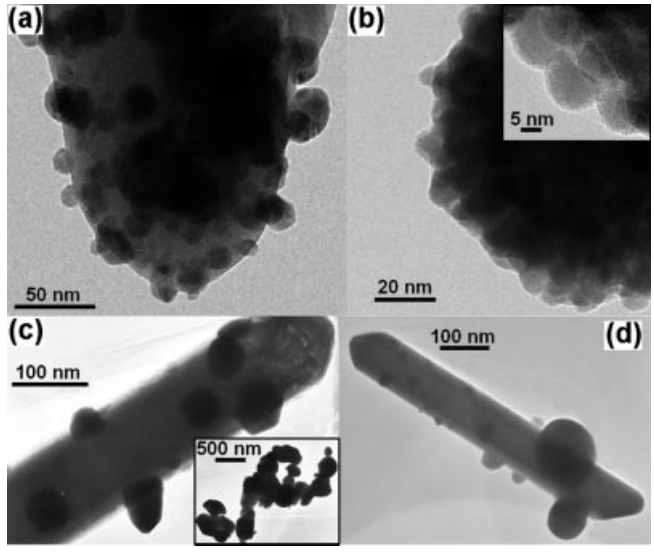

Figure 2. (a) Aggregation and growth of Ag nanoparticles with increased sonication time (120 min; after calcination to 450 °C). (b) TEM micrograph of the tip of a α-$Bi_2Mo_3O_{12}$ nanorod with deposited Ag nanoparticles, showing the nature of deposition and morphology of deposited Ag nanoparticles when 300 mg of Ag_2O was used. Inset shows an HRTEM image. (c) TEM image of randomly deposited Ag_2O nanoparticles on α-$Bi_2Mo_3O_{12}$ nanorods obtained after stirring the mixture of Ag_2O and α-$Bi_2Mo_3O_{12}$ nanorods in pyridine at 40 °C. Inset shows TEM image of a chain of large Ag_2O nanoparticles observed in the product. (d) Representative TEM micrograph of a nanorod obtained on heating the homogenized mixture of Ag_2O and α-$Bi_2Mo_3O_{12}$ nanorods at a controlled rate of 5 °C min^{-1}.

product, as shown in the inset in Figure 2c. These might be due to the fusion of free Ag_2O particles during the calcination process. In contrast, when a homogenized mixture of Ag_2O and α-$Bi_2Mo_3O_{12}$ nanorods is heated to 450 °C in the absence of pyridine and at a controlled heating rate of 5 °C min^{-1}, very few Ag_2O particles of varying size are seen bound to the surface of the nanorods, as shown in Figure 2d. Furthermore, the XRD pattern (Figure 4e) obtained from the product shows a change in composition and the pattern is observed to be in good agreement with that of $AgBi(MoO_4)_2$ (JCPDS 32-0999).

Thermal Analysis

TG-DTG thermograms recorded in the temperature range from 30 to 500 °C with a heating rate of 5 °C min^{-1} in a flow of air at 20 mL min^{-1} using pyridine-intercalated α-$Bi_2Mo_3O_{12}$ nanorods are shown in Figure 3a and 3a′and those of α-$Bi_2Mo_3O_{12}$ nanorods with deposited Ag nanoparticles are shown in Figure 3b and b′. The TG thermogram (Figure 3a) recorded from pyridine-intercalated α-$Bi_2Mo_3O_{12}$ nanorods shows a weight loss of 5% and can be attributed to the loss of pyridine. The respective DTG thermogram (Figure 3a′), which is derivative of the TG thermogram, shows dips at 187, 245 and 314 °C, which indicates that the weight loss takes place in three steps. The deintercalation process extends up to 400 °C and no further weight loss is observed at higher temperatures. The TG thermogram (Figure 3b) recorded from α-$Bi_2Mo_3O_{12}$ nanorods with deposited Ag nanoparticles shows a weight loss of 8.8% due to loss of pyridine. The desorption and deintercalation process extends up to 450 °C, slightly higher than that observed in the earlier thermogram, which might be due to the deposited silver nanoparticles. Moreover, the observed weight loss is also higher and can be attributed to the loss of pyridine adsorbed on Ag nanoparticles in addition to loss of pyridine intercalated in α-$Bi_2Mo_3O_{12}$ nanorods. The respective DTG thermogram (Figure 3b′) shows a sharp dip at 90.1 °C and can be attributed to desorption of pyridine adsorbed on Ag nanoparticles. The two broad dips at 209 and 314 °C might be due to slow elongated deintercalation of pyridine from the product because of the deposited Ag nanoparticles on the surface.

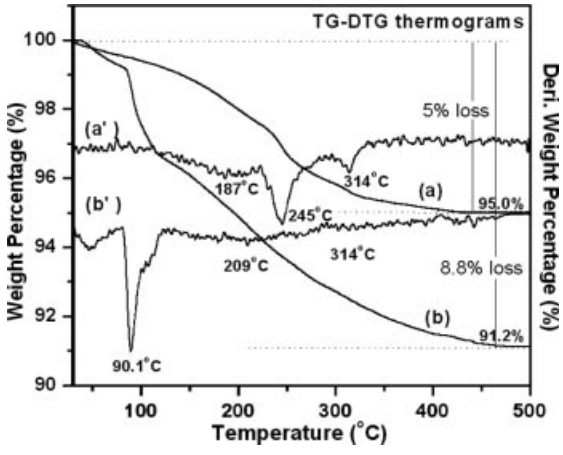

Figure 3. (a) TG thermogram obtained from pyridine-intercalated α-$Bi_2Mo_3O_{12}$ nanorods and (a′) its DTG thermogram. (b) TG thermogram obtained from α-$Bi_2Mo_3O_{12}$ nanorods with deposited Ag nanoparticles obtained after sonication for 60 min with 100 mg Ag_2O and (b′) its DTG thermogram.

X-ray Diffraction

The XRD patterns of the product and intermediates are shown in Figure 4. Representative XRD patterns of $Bi_2Mo_3O_{12}\cdot 5H_2O$ shown in Figure 4a can be indexed to a monoclinic cell with lattice parameters of a = 6.334, b = 11.593, c = 5.777 Å and β = 113.166° (JCPDS 41-0361), even though the formula is given to be $Bi_2Mo_3O_{12}\cdot 4.75H_2O$. The XRD pattern is also observed to be in close agreement with that reported by Barnes et al.,[21] even though they claimed the correct formula to be $BiMo_2O_7OH\cdot 2H_2O$. However, our EDS analysis is in accordance with the expected Bi/Mo ratio of 2:3 and also the TG analysis shows weight loss corresponding to five molecules of water.[26] The XRD pattern obtained from spherical nanoparticles of α-$Bi_2Mo_3O_{12}$ phase as shown in Figure 4b is in close agreement with that reported by Li and Cheng[27] and in a literature report (JCPDS 70-1396). The crystal structure of α-$Bi_2Mo_3O_{12}$ phase (scheelite structure) is reported to be monoclinic, trigonal-bipyramidal or distorted tetrahedral with space group $P2_1/c$ and cell parameters a = 7.685, b = 11.491 and c = 11.929 Å and characteristic edge β = 115.40°. The XRD pattern of pyridine-intercalated α-$Bi_2Mo_3O_{12}$ nanorods is shown in Figure 4c. It exhibits some similarities with that of pure α-$Bi_2Mo_3O_{12}$ phase (Figure 4b) owing to the use of α-$Bi_2Mo_3O_{12}$ as the starting material for pyridine intercalation. The peaks observed at lower 2θ values are indicative of an increased interlayer region due to pyridine intercalation similar to that reported earlier.[19,21] The peaks appear to be broad, probably because of the reduced particle size and intercalation of pyridine. To the best of our knowledge, the reference database file (JCPDS) does not exist, as most of the researchers used the hydrated form of $Bi_2Mo_3O_{12}$ for pyridine intercalation studies, as discussed in an earlier report.[16] The XRD pattern of α-$Bi_2Mo_3O_{12}$ nanorods with deposited Ag nanoparticles (Figure 4d) is different from its counterpart in the sense that it shows characteristic peaks at 2θ = 38.04°, 44.22° and 64.36° that could be indexed to [111], [200] and [220] reflection lines, respectively, of FCC Ag particle (JCPDS 04-0783). Traces of less intense peaks indicative of cubic Ag_2O (JCPDS 75-1532) are also observed and can be attributed to the surface oxidation of Ag nanoparticles. The XRD pattern obtained from slow controlled heating of a homogenized mixture of α-$Bi_2Mo_3O_{12}$ nanorods and Ag_2O is shown in Figure 4e. The pattern is in good agreement with that reported for $AgBi(MoO_4)_2$ (JCPDS 32-0999) and different from that observed for α-$Bi_2Mo_3O_{12}$ nanorods with deposited Ag nanoparticles. This indicates a change in composition during solid-state reaction as a result of diffusion of Ag atoms, which

alter the composition during the heating process. It is interesting to note that the α-$Bi_2Mo_3O_{12}$ nanorods with deposited Ag nanoparticles (Figure 4d) do not show diffusion of Ag or change in composition. This might be due to intercalated pyridine preventing the diffusion of Ag, as diffusion and deintercalation processes are expected to occur at the same time during heating.

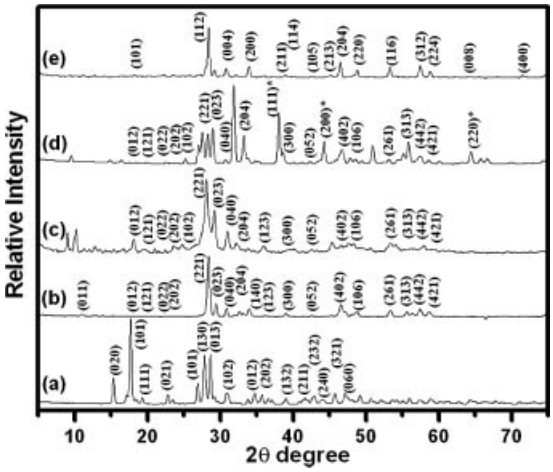

Figure 4. XRD spectra of (a) $Bi_2Mo_3O_{12}·5H_2O$, (b) α-$Bi_2Mo_3O_{12}$, (c) pyridine-intercalated α-$Bi_2Mo_3O_{12}$ nanorods, (d) α-$Bi_2Mo_3O_{12}$ nanorods with deposited Ag nanoparticles obtained after sonication for 60 min with 100 mg Ag_2O and (e) product obtained from heating the homogenized mixture of Ag_2O and α-$Bi_2Mo_3O_{12}$ nanorods.

X-ray Photoelectron Spectroscopy

An XPS surface scan spectrum of α-$Bi_2Mo_3O_{12}$ nanorods with deposited Ag nanoparticles is shown in Figure 5. It shows characteristic peaks for $Mo3d_{5/2}$ (233 eV), $Mo3d_{3/2}$ (235.8 eV), $Bi4f_{7/2}$ (160 eV) and $Bi4f_{5/2}$ (165 eV). XPS analysis did not detect any modification in the atomic ratio or Mo oxidation state of the Ag-nanoparticle-deposited α-$Bi_2Mo_3O_{12}$ nanorods compared to those of α-$Bi_2Mo_3O_{12}$. However, a considerable shift in the $Bi4f_{5/2}$ peak is observed, probably because of the change in oxidation state of Bi. It is well known that there is a strong interaction between Bi and Ag, and thus, it is expected that the deposited Ag nanoparticles would prefer Bi sites rather than Mo for binding on the surface. Reports on the presence of stable Ag–Bi alloys support our speculation.[12,13] To further confirm this possibility, TOF-SIMS analysis and TOF-SIMS imaging were also conducted.

TOF-SIMS

Figure 6 shows a positive TOF-SIMS spectrum of α-$Bi_2Mo_3O_{12}$ nanorods with deposited Ag nanoparticles. A typical TOF-SIMS spectrum in positive-ion mode shows the presence of characteristic ions of $^{98}Mo^+$ (m/z = 98), MoO^+ (m/z = 114), $^{209}Bi^+$ (m/z = 209), $^{107}Ag^+$ (m/z = 107) and $^{109}Ag^+$ (m/z = 109) supporting the deposition of Ag nanoparticles on the surface of α-$Bi_2Mo_3O_{12}$ phase nanorods. Additionally, ions corresponding to Na^+ and K^+ as trace impurities were also observed. The absence of ions corresponding to pyridine indicates the complete removal of pyridine on heating at 450 °C. The high-intensity peaks $^{107}Ag^+$ and $^{109}Ag^+$ confirm the major composition of Ag nanoparticles deposited on the surface of α-$Bi_2Mo_3O_{12}$ nanorods. No more information with regards to the site or nature of binding of the Ag nanoparticles could be extracted and thus TOF-SIMS imaging is also performed.

To investigate the dispersion and binding site of Ag nanoparticles on the surface of α-$Bi_2Mo_3O_{12}$ nanorods, secondary-ion images characteristic of Bi, Mo and Ag were obtained. Figure 7 shows secondary-ion images of individual elemental components (a) $^{209}Bi^+$, (b) $^{98}Mo^+$, (c) $^{107}Ag^+$ and (d) $^{109}Ag^+$ obtained from Ag-nanoparticle-deposited α-$Bi_2Mo_3O_{12}$ nanorods that were sonicated for 60 min. The two-component total-ion images of $^{209}Bi^+$ and $^{107}Ag^+$ (Figure 7e), and $^{98}Mo^+$ and $^{109}Ag^+$ (Figure 7f) were also recorded for comparison. The bright spots in the image indicate the presence of characteristic metal species. Homogen-

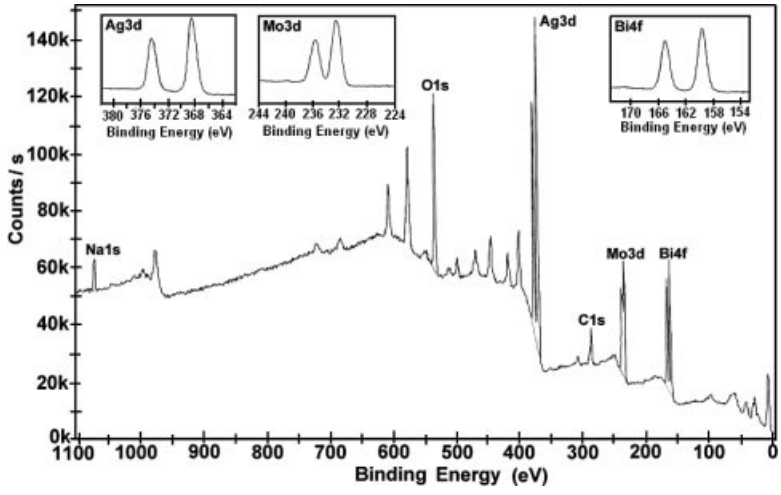

Figure 5. XPS spectrum measured on α-$Bi_2Mo_3O_{12}$ nanorods with deposited Ag nanoparticles.

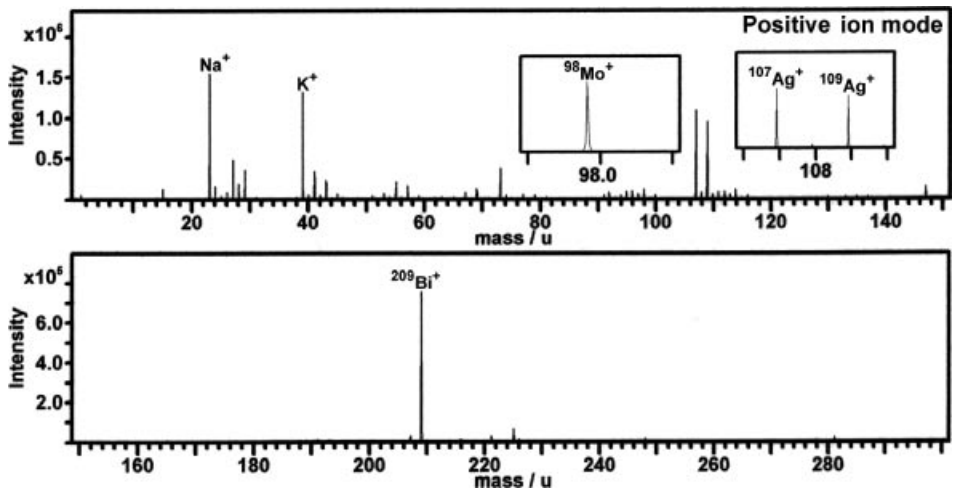

Figure 6. TOF-SIMS spectra of α-$Bi_2Mo_3O_{12}$ nanorods with deposited Ag nanoparticles in positive-ion detection mode.

eous distribution of Bi and Mo is observed (Figure 7a and b). However, the ion images of $^{107}Ag^+$ and $^{109}Ag^+$ show significant overlap with $^{209}Bi^+$, as depicted from the bright spots in the pattern of Figure 7a, b, d and e. In other words, the image pattern characteristic of Bi and that of Ag are similar. This supports our speculation that Bi might be the preferred site for deposition of Ag nanoparticles on the surface of α-$Bi_2Mo_3O_{12}$ nanorods. The fact that the Ag nanoparticles are dispersed on the surface suggests that Bi is localized on the α-$Bi_2Mo_3O_{12}$ nanorods, maintaining the compositional structure of the nanorods.

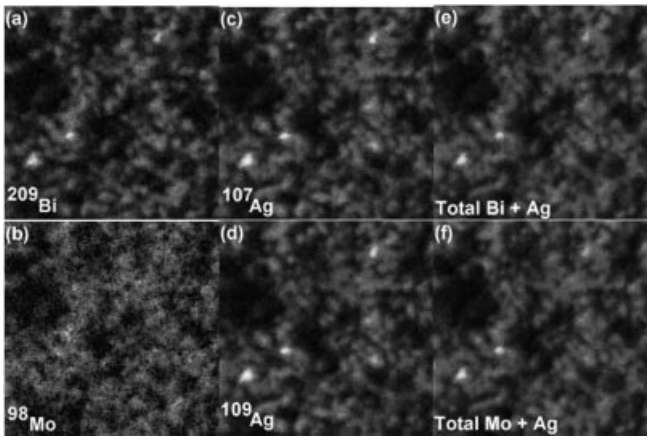

Figure 7. TOF-SIMS images of characteristic elements: (a) $^{209}Bi^+$, (b) $^{98}Mo^+$, (c) $^{107}Ag^+$ and (d) $^{109}Ag^+$ from α-$Bi_2Mo_3O_{12}$ nanorods with deposited Ag nanoparticles. Two-component total-ion images of (e) $^{209}Bi^+$ and $^{107}Ag^+$ and (f) $^{98}Mo^+$ and $^{109}Ag^+$.

Proposed Mechanism

Sonication of Ag_2O in pyridine results in the formation of Ag nanoparticles of about 10 nm (inset in Figure 1b) and subsequently pyridine is adsorbed on the surface. Similarly, synthesis and crystal growth of uniform Ag nanoplates and ring-like gold nanocrystals in *N*,*N*-dimethylformamide solution were reported by using the sonochemical route.[28] The pyridine-adsorbed Ag nanoparticles eventually align in the vicinity of pyridine-adsorbed α-$Bi_2Mo_3O_{12}$ nanorods through π stacking interactions of surface-adsorbed pyridine. The adsorption and intercalation of pyridine is confirmed by thermogravimetric analysis. Further, with the implosive collapse of bubbles in the liquid due to ultrasonic irradiation, the Ag nanoparticles deposit on the surface of the α-$Bi_2Mo_3O_{12}$ nanorods and form a Ag-nanoparticle-deposited α-$Bi_2Mo_3O_{12}$ nanorod and pyridine nanocomposite. The uniform deposition of Ag nanoparticles on the surface might be due to the presence of adsorbed pyridine on the Ag nanoparticles, which would prevent aggregation.

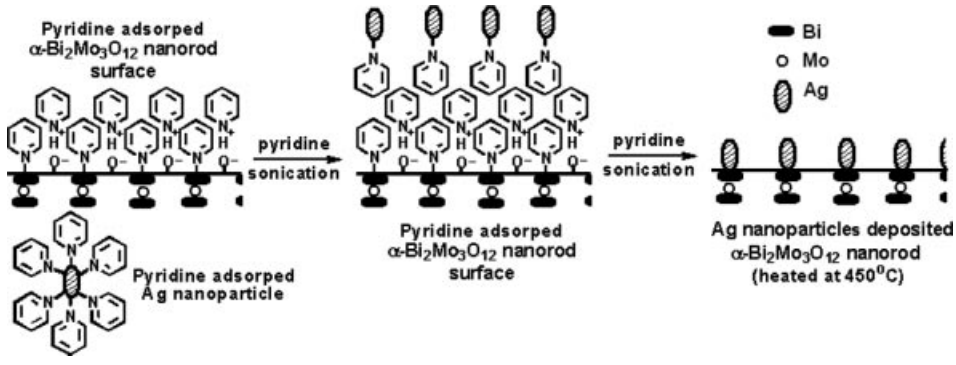

Figure 8. Schematic diagram for the proposed mechanism producing α-$Bi_2Mo_3O_{12}$ nanorods with deposited Ag nanoparticles.

With the use of increased amounts of Ag_2O, the deposition of Ag nanoparticles was found to increase; the particles were localized in close vicinity to each other on the surface of the α-$Bi_2Mo_3O_{12}$ nanorods, with less aggregation, and the particles maintained their size. The particles seem to deposit in the voids of the Ag nanoparticles instead of collapsing on the previously deposited Ag nanoparticles, probably because of surface-adsorbed pyridine. However, it was observed that an increased sonication time forces the collapse of the Ag nanoparticles and the formation of aggregates of Ag nanoparticles on the surface. Further, calcination of the nanocomposite at 450 °C results in pyridine-free, Ag-nanoparticle-deposited α-$Bi_2Mo_3O_{12}$ nanorods. A schematic diagram of the proposed mechanism is shown in Figure 8.

Conclusions

Silver nanoparticles are uniformly deposited on the surface of α-$Bi_2Mo_3O_{12}$ nanorods by using a simple ultrasonication method. The Ag nanoparticles disperse well in pyridine and bind to the surface of nanorods under the influence of the liquid bubbles generated by ultrasound in the pyridine medium, forming a nanocomposite of α-$Bi_2Mo_3O_{12}$ nanorods with deposited Ag nanoparticles, and pyridine. Adsorption and intercalation of pyridine prevents aggregation and diffusion of Ag nanoparticles. By heating the sample at 450 °C, the formation of a pyridine-free nanocomposite with deposited crystalline Ag nanoparticles is observed. Thorough characterization using TEM, SAED, EDS, XRD, XPS and TOF-SIMS was carried out to confirm the presence of crystalline Ag nanoparticles. Additionally, the use of TOF-SIMS imaging could provide information with regards to the possible binding site of the Ag nanoparticles on the surface of the α-$Bi_2Mo_3O_{12}$ nanorods. These Ag-nanoparticle-deposited α-$Bi_2Mo_3O_{12}$ nanorods might find applications in catalysis.

Experimental Section

Bi_2O_3 (Aldrich, 99%), $Na_2MoO_4{\cdot}2H_2O$ (Riedel-de Haën, 99%), Ag_2O (Showa, 98%) and pyridine (Fluka, >99%) were purchased and used without further purification.

Large spherical nanoparticles of α-$Bi_2Mo_3O_{12}$ (ca. 200 nm size) were prepared as discussed in our earlier report.[16,26] The resultant α-$Bi_2Mo_3O_{12}$ product (2 g in each experiment) was further treated with an excess of pyridine (10 mL), and sonicated at 30–40 °C by using a fixed power sonicator (L&R Ultrasonics, Quantrex 140, 150 W, 45 kHz) under a nitrogen atmosphere for 60 min to produce α-$Bi_2Mo_3O_{12}$ nanorods (ca. 100 nm diameter). The excess pyridine was vacuum evaporated, followed by an acetone wash and dried at 60 °C. Compositional and morphological characterization of nanorods was performed thereafter. Thermal treatment (calcination) of the nanocomposite at 450 °C removed the residual pyridine and afforded pyridine-free nanorods of α-$Bi_2Mo_3O_{12}$. The morphological features of the nanorods thus obtained did not vary from those of the intercalated product, similar to those observed in our earlier report.[16] The deposition of Ag nanoparticles on the surface of α-$Bi_2Mo_3O_{12}$ nanorods was conducted by sonicating the mixture of Ag_2O (100 mg) and α-$Bi_2Mo_3O_{12}$ nanorods (2 g) in the presence of pyridine for 60 min. Alternatively, the same results were obtained when α-$Bi_2Mo_3O_{12}$ nanorods formed after sonication in pyridine (from α-$Bi_2Mo_3O_{12}$ nanoparticles) were subsequently treated with Ag_2O (100 mg) and further sonicated for 60 min. The Ag_2O used was free of trace amounts of elemental silver. Experiments with an increased sonication time (60, 90 and 120 min) and the use of different amounts of Ag_2O (100, 200 and 300 mg) were also conducted. Prior to characterization, the final product was washed, dried and calcinated by using the same protocol as mentioned earlier. Furthermore, to prove the effect of ultrasound in uniform deposition of Ag nanoparticles on α-$Bi_2Mo_3O_{12}$ nanorods, a contrast experiment involving controlled heating (5 °C min^{-1}) of a homogenized mixture of pyridine-free α-$Bi_2Mo_3O_{12}$ nanorods (2 g) and Ag_2O (100 mg) was conducted. The mixture was heated to 450 °C and cooled naturally. An additional experiment involving vigorous stirring of a mixture of α-$Bi_2Mo_3O_{12}$ nanorods (2 g) and Ag_2O (100 mg) in pyridine (10 mL) at 40 °C for 60 min in nitrogen was also conducted.

A thermogravimetric analyzer (Perkin–Elmer TGA6) was used to record the thermograms in the temperature range 30–500 °C with a heating rate of 5 °C min^{-1} in a flow of air at 20 mL min^{-1}. Morphological characterization was performed using a transmission electron microscope (TEM) (Philips, Tecnai 20) working at 200 kV accelerating voltage. A drop of sample suspension, which had been previously dispersed in methanol by ultrasonication, was placed on the Cu microgrid coated with lacey carbon film and dried before microscopy study. Elemental composition was obtained by energy-dispersive X-ray analysis (EDS) (Philips, Tecnai 20). Scanning electron microscope (SEM) (Hitachi-S4700, Noran Instruments) was also employed. The samples in powder form were dispersed on the carbon tape mounted on the sample holder and an epitaxial thin film of platinum was coated (plasma coating technique) on the sample surface to avoid surface charging problems. The X-ray diffraction (XRD) patterns were obtained using Material Analysis and Characterization (MAC) advanced powder X-ray diffractometer (using Cu-K_α = 1.54056 Å radiation) and scanning in the 2θ range between 5° and 100° at a rate of 0.25° min^{-1}. An X-ray photoelectron spectrometer (Thermo VG Scientific) with monochromatized Al-K_α X-ray (1486.6 eV) source and a spherical capacitor analyzer with multichannel detector was used for surface composition study. The samples were pressed into pellets and mounted on a standard sample holder using conductive carbon tape. The vacuum in the analysis chamber was maintained at 10^{-9} Torr. A total of 10–30 scans were collected from the spot size of 400 μm, with an energy step of 1 eV and pass energy of 100 eV. A detailed surface composition of metal deposits was obtained by analysis of Ag3d, Mo3d, Bi4f, O1s and C1s peaks.

TOF-SIMS (ION-TOF; Munich, Germany) measurements in positive-ion mode were performed for the analysis of α-$Bi_2Mo_3O_{12}$ nanorods and Ag-nanoparticle-deposited α-$Bi_2Mo_3O_{12}$ nanorods. The samples were pressed onto the carbon tape supported on a clean Si wafer. Excess particles were removed by blowing with compressed air such that the layer thickness was minimal, but large enough to prevent exposure of the carbon tape. The primary-ion source was a pulsed $^{69}Ga^+$ source (pulsing current 2.5 pA, and a pulse width of 30 ns) operated at 15 keV with postacceleration of 10 kV. An analysis area of 100 × 100 μm, data acquisition time of 200 s and charge compensation by applying low-energy electrons (ca. 30 eV) from a pulsed flood gun were used for the measurements. The pressure of the main chamber was kept between 10^{-8} and 10^{-9} Torr. The best resolution obtained was $m/\Delta m$ = 8000.

Calibration of the mass spectra was based on peaks such as H^+ (1.007 *m*/*z*), CH_3^+ (15.024 *m*/*z*), $C_2H_5^+$ (29.044 *m*/*z*), Mo^+ (97.908 *m*/*z*), $^{107}Ag^+$ (106.907 *m*/*z*), $^{109}Ag^+$ (108.906 *m*/*z*) and Bi^+ (208.983 *m*/*z*), and the peak areas were normalized to the most intense peak in the spectrum. The generated data were processed using inbuilt IonSpec and Ionimage software.

Acknowledgments

Financial support by National Science Council (NSC94-2218-E-007-052) and National Tsing Hua University is gratefully acknowledged.

[1] a) G. R. Patzke, F. Krumeich, R. Nesper, *Angew. Chem. Int. Ed.* **2002**, *41*, 2446–2461; b) Y. Xia, P. Yang, Y. Sun, Y. Wu, B. Mayers, B. Gates, Y. Yin, F. Kim, H. Yan, *Adv. Mater.* **2003**, *15*, 353–389; c) M. Alexandre, P. Dubois, *Mater. Sci. Eng.* **2000**, *28*, 1–63.

[2] a) T. E. Crumpton, C. Greaves, *J. Mater. Chem.* **2004**, *14*, 2433–2437; b) Z. Ban, J. He, G. Vladimir, W. Wang, C. J. O'Connor, *J. Mater. Chem.* **2005**, *15*, 1244–1247; c) P. Christian, P. O'Brien, *J. Mater. Chem.* **2005**, *15*, 3021–3025; d) M. H. Tran, H. Ohkita, T. Mizushima, N. Kakuta, *Appl. Catal. A* **2005**, *287*, 129–134; e) K. A. Gesheva, T. Ivanova, F. Hamelmann, *J. Optoelectronics Adv. Mater.* **2005**, *7*, 1243–1252.

[3] a) A. M. Beale, G. Sankar, *Chem. Mater.* **2003**, *15*, 146–153; b) E. Godard, E. M. Gaigneaux, P. Ruiz, B. Delmon, *Catal. Today* **2000**, *61*, 279–285; c) N. Arora, G. Deo, I. E. Wachs, A. M. Hirt, *J. Catal.* **1996**, *159*, 1–13.

[4] a) R. N. Vannier, F. Abraham, G. Nowogrocki, G. Mairesse, *J. Solid State Chem.* **1999**, *142*, 294–304; b) L. Boon, R. Metselaar, *Eur. J. Solid State Inorg. Chem.* **1990**, *27*, 381–389.

[5] V. Marinova, M. Veleva, *Opt. Mater.* **2002**, *19*, 329–333.

[6] K. Y. Kang, P. H. Her, M. S. Jang, H. K. Kim, H. L. Park, D. Finotello, M. H. W. Chan, *Solid State Commun.* **1988**, *67*, 723–724.

[7] T. Sekiya, A. Tsuzuki, Y. Torii, *Mater. Res. Bull.* **1985**, *21*, 601–608.

[8] N. Hykaway, W. M. Sears, R. F. Frindt, S. R. Morrison, *Sens. Actuators* **1988**, *15*, 105–118.

[9] a) J. H. Fendler, *Nanoparticles and Nanostructured Films: Preparation, Characterization and Applications*, John Wiley & Sons, New York, **1998**; b) J. Jose, M. A. Khadar, *Acta Mater.* **2001**, *49*, 729–735; c) L. Kutsenko, D. Fuks, A. Kiv, L. Burlaka, M. Talianker, O. Monteiro, I. Brown, *Acta Mater.* **2004**, *52*, 4329–4335.

[10] a) Y. Shiraishi, N. Toshima, *J. Mol. Catal. A: Chem.* **1999**, *141*, 187–192; b) J. G. Serafin, A. C. Liu, S. R. Seyedmonir, *J. Mol. Catal. A: Chem.* **1998**, *131*, 157–168; c) S. Imamura, M. Ikebata, T. Ito, T. Ogita, *Ind. Eng. Chem. Res.* **1991**, *30*, 217–221.

[11] a) B. M. Luce, D. G. Foulke, *Modern Electroplating*, 3rd ed., John Wiley and Sons, New York, **1974**; b) K. Chatterjee, J. M. Howe, W. C. Johnson, M. Murayama, *Acta Mater.* **2004**, *52*, 2923–2935; c) S. V. Divinski, F. Hisker, Y. S. Kang, J. S. Lee, C. Herzig, *Acta Mater.* **2004**, *52*, 631–645; d) I. Krastev, T. Valkova, A. Zielonka, *J. Appl. Electrochem.* **2003**, *33*, 1199–1204.

[12] I. Krastev, T. Valkova, A. Zielonka, *J. Appl. Electrochem.* **2004**, *34*, 79–85.

[13] R. Regnier, C. Bifulco-Michon, F. Legendre, S. Poissonnet, G. Giunchi, *Physica C* **2002**, *372–376*, 923–926.

[14] Q. Li, H. Li, V. G. Pol, I. Bruckental, Y. Koltypin, J. Calderon-Moreno, I. Nowik, A. Gedanken, *New J. Chem.* **2003**, *27*, 1194–1199.

[15] a) V. G. Pol, A. Gedanken, J. Calderon-Moreno, *Chem. Mater.* **2003**, *15*, 1111–1118; b) V. G. Pol, O. Palchik, A. Gedanken, I. Felner, *J. Phys. Chem. B* **2002**, *106*, 9737–9743; c) V. G. Pol, M. Motiei, A. Gedanken, J. Calderon-Moreno, Y. Mastai, *Chem. Mater.* **2003**, *15*, 1378–1384.

[16] A. V. Ghule, K. A. Ghule, S. H. Tzing, J. Y. Chang, H. Chang, Y. C. Ling, *Chem. Phys. Lett.* **2004**, *383*, 208–213.

[17] K. S. Suslick (Ed.), *Ultrasound: Its Chemical, Physical and Biological Effects*, VCH, Weinheim, Germany, **1988**.

[18] Y. Socol, O. Abramson, A. Gedanken, Y. Meshorer, L. Berenstein, A. Zaban, *Langmuir* **2002**, *18*, 4736–4740.

[19] Y. Murakami, H. Imai, *J. Mater. Sci. Lett.* **1990**, *10*, 107–108.

[20] S. Yinjie, Z. Aimin, *J. Radioanal. Nucl. Chem.* **1998**, *231*, 17–20.

[21] N. Barnes, S. J. Kitchin, J. A. Hriljac, *Inorg. Chem.* **1999**, *38*, 6317–6319.

[22] A. V. Ghule, C. Y. Chen, F. D. Mei, Y. C. Ling, *Appl. Surf. Sci.* **2004**, *231–2*, 840–844.

[23] a) Y. E. Cho, J. Y. Maeng, S. Kim, *J. Am. Chem. Soc.* **2003**, *125*, 7514–7515; b) E. Lust, A. Janes, P. Miidla, K. Lust, *J. Electroanal. Chem.* **1997**, *425*, 25–37; c) D. Y. Wu, M. Hayashi, Y. J. Shiu, K. K. Liang, C. H. Chang, Y. L. Yeh, S. H. Lin, *J. Phys. Chem. A* **2003**, *107*, 9658–9667.

[24] M. I. Zaki, M. A. Hasan, F. A. Al-Sagheer, L. Pasupulety, *Colloids Surf., A* **2001**, *190*, 261–274.

[25] a) H. N. Kwok, H. Liu, R. M. Penner, *Langmuir* **2000**, *16*, 4016–4023; b) R. M. Stiger, S. Gorer, B. Craft, R. M. Renner, *Langmuir* **1999**, *15*, 790–798.

[26] A. V. Ghule, S. H. Tzing, J. Y. Chang, K. A. Ghule, H. Chang, Y. C. Ling, *Eur. J. Inorg. Chem.* **2004**, 1753–1762.

[27] K. T. Li, W. D. Cheng, *Appl. Catal., A* **1996**, *142*, 315–326.

[28] L. P. Jiang, S. Xu, J. M. Zhu, J. R. Zhang, J. J. Zhu, H. Y. Chen, *Inorg. Chem.* **2004**, *43*, 5877–5883.

Received: February 7, 2007
Published Online: May 30, 2007

